

Construction of MoO₃/MoSe₂ nanocomposite based gas sensor for low detection limit trimethylamine sensing at room temperature

Lanjuan Zhou

China University of Petroleum Huadong - Qingdao Campus

Qian Mi

China University of Petroleum Huadong - Qingdao Campus

Yingbo Jin

China University of Petroleum Huadong - Qingdao Campus

Tingting Li (✉ litington0406@163.com)

China University of Petroleum Huadong - Qingdao Campus <https://orcid.org/0000-0001-5272-4551>

Dongzhi Zhang

China University of Petroleum Huadong - Qingdao Campus

Research Article

Keywords: Molybdenum trioxide, Hydrothermal method, TMA sensor, MoO₃/MoSe₂ heterostructure

Posted Date: March 22nd, 2021

DOI: <https://doi.org/10.21203/rs.3.rs-336116/v1>

License: © ⓘ This work is licensed under a Creative Commons Attribution 4.0 International License.

[Read Full License](#)

Abstract

In this paper, MoO₃/MoSe₂ n-n heterostructure was constructed for fabricating trimethylamine (TMA) gas sensor by an improved hydrothermal and spin-coating method. The surface morphology and microstructure of the prepared materials were analyzed by XRD, XPS, SEM and TEM characterization methods. The microstructural characterization results demonstrated that the MoO₃/MoSe₂ heterostructure had been successfully synthesized, in which the MoSe₂ had a flower-shaped structure, and MoO₃ had a rod-shaped structure. At the same time, the MoSe₂ surface exhibited periodic honeycomb structure. The gas-sensitivity experimental results showed that the proposed MoO₃/MoSe₂ sensor had excellent TMA sensing performance at room temperature, including high response capability, low detection limit (20 ppb), short response/recovery time (12 s/19 s), long-term stability, good repeatability and outstanding selectivity. The heterostructure of MoO₃/MoSe₂ had made outstanding contributions to the enhanced TMA gas sensing performance at room temperature.

1. Introduction

Trimethylamine (TMA) is a kind of colorless gas, whose vapor can form explosive mixture in air, and it will burn and explode violently when exposed to open flames or high heat, resulting in toxic smoke after thermal decomposition, which poses a great threat to human safety. Human exposure to TMA can cause severe irritation to eyes, nose and skin, and even affect the nervous system [1]. The American Conference of Governmental Industrial Hygienists recommend that the TMA concentrations of people exposed to for long and short periods should not exceed 5 and 15 ppm, respectively [2]. Interestingly, fresh fish meat contains umami trimethylamine oxide. After the fish dies, trimethylamine oxide is easily reduced to trimethylamine, and trimethylamine makes the fish smell stench [3 – 4]. In life, TMA can be used as a biomarker to assess the freshness of fish and other seafood. Seafood with a TMA concentration exceeding 10 ppm is evaluated as rotten [5 – 6]. In addition, patients with trimethylaminuria have congenital inability to metabolize trimethylamine, who will release it through breathing, urine and sweat, thus resulting patients with fishy smell. Therefore, TMA is expected to play a role in disease diagnosis. Overall, the development of TMA sensors is essential for air quality detection and human health monitoring.

As a typical n-type semiconductor, molybdenum trioxide (MoO₃) is an important candidate material in gas sensing [7 – 10]. Especially when detecting TMA, because the surface of MoO₃ contains a large number of lewis acid sites, it can react strongly with alkaline TMA [11]. For example, Yang et al. prepared ultra-long flexible MoO₃ nanoribbons. MoO₃ nanoribbons gas sensor had good selectivity for trimethylamine, and the response to 50 ppm TMA was 582 (240°C) [12]. Shen et al. synthesized two-dimensional (2D) ultra-thin α -MoO₃ nanosheets with oxygen vacancies, with porous surface of 2 – 10 nm pore size. At a relatively low operating temperature (133°C), the response of α -MoO₃ nanosheets gas sensor to 50 ppm TMA was 198 and the detection limit was 20 ppb [6]. As we all know, sensor performance is largely due to the morphology of the metal oxide. Compared with other nanostructures,

one-dimensional (1D) nanostructure has larger specific surface area. Therefore, super-dispersed ultra-long MoO_3 nanorods were synthesized by an improved hydrothermal method. In addition, TMA sensors based on MoO_3 usually require higher operating temperature, resulting in high power consumption and potential safety hazards, so it is necessary to dope other semiconductors to improve the sensing performance.

2D layered material molybdenum selenide (MoSe_2) has attracted great attention because of its well-known semiconductor properties. MoSe_2 is widely used especially as catalyst [13 – 16] and electrode material [17 – 19]. In addition, MoSe_2 also shows superior performance in the field of gas sensing. For example, Zhang et al. used MoSe_2 nanosheets by liquid phase exfoliation as starting materials, and prepared MoSe_2 nanosheets with controllable lateral dimension by controlling the centrifugal condition, which provided basis for the study of relationship between sensing characteristics and material sizes. The results showed that MoSe_2 nanosheets have more competitive advantages than traditional graphene-based sensors [20]. Also using the convenient method of liquid phase exfoliation, the MoSe_2 nanosheets exfoliated by Chen et al. had significantly enhanced NO_2 detection performance. Sensor response to 10 ppm NO_2 was 1500%, 18 times the original MoSe_2 , and the detection limit was as low as 50 ppb, while showed excellent selectivity and stability, making MoSe_2 nanosheets a good choice for NO_2 sensors at room temperature (RT) [21]. Zhang et al. synthesized Pd- MoSe_2 thin film sensor by modifying MoSe_2 nanoflowers with Pd, confirming that Pd-decorated MoSe_2 nanoflowers were good choice for RT NH_3 detection [22].

In order to solve the problem of high power consumption of MoO_3 and improve the gas-sensing performances, room temperature TMA sensor based on heterostructure of MoSe_2 nanoflower-modified MoO_3 was prepared by a simple hydrothermal method. The microstructure and surface morphology of the samples were investigated by a series of characterization techniques such as XRD, XPS, SEM and TEM. For the sake of further investigating the effect of the synergy of the two materials on sensing properties, the relevant gas sensing experiments of single MoSe_2 and $\text{MoO}_3/\text{MoSe}_2$ were also conducted. The results showed that compared with single sensing material, the $\text{MoO}_3/\text{MoSe}_2$ composite-based sensor exhibited more excellent sensing properties to TMA in terms of selectivity, sensitivity, response/recovery time and minimum detection limit. At the same time, the sensing mechanism was also explained in detail based on the theory of oxygen adsorption and desorption on the semiconductor surface and n-n heterostructure theory.

2. Experiment

2.1 Materials

Molybdenum powder, selenium powder, sodium borohydride (NaBH_4), sodium molybdate ($\text{Na}_2\text{MoO}_4 \cdot 2\text{H}_2\text{O}$), H_2O_2 and ethanol were purchased by Sinopharm Chemical Reagent (Shanghai, China).

2.2 Materials synthesis

2.2.1 Synthesis of MoO₃ nanorods

The ultra-long MoO₃ nanorods were synthesized by an improved hydrothermal method. Firstly, 2 g of molybdenum powder was added into 10 mL deionized water (DI) with thorough mixing. Then, 20 mL of H₂O₂ was slowly added to the above solution until it became pale yellow, and stirring was continued for 30 min to make reaction thorough. After that, the resulting solution was transferred to a 50 mL autoclave, then heated to 220°C and maintained for 48 h [23]. Finally, after the reactor was cooled to RT, the precipitate was filtered and washed with DI and ethanol for several times to remove impurities, thereby obtaining pure MoO₃ suspension.

2.2.2 Synthesis of MoSe₂ nanoflowers

The hydrothermal method was also used to synthesize MoSe₂ nanoflowers. Firstly, 0.493 g of selenium powder was dissolved in 10 mL hydrazine hydrate solution. Then, the dissolved Se powder solution, 0.1 g of NaBH₄, 0.6 g of Na₂MoO₄·2H₂O and 25 mL of ethanol were added into 25 mL DI, and continued stirring for 1 h. Next, the resulting mixture was transferred to a 100 mL autoclave and heated at 200°C for 48 h. Finally, DI was used to wash and filter the obtained black fluffy material to remove excess impurity ions, thereby obtaining pure MoSe₂ suspension.

2.2.3 Synthesis of MoO₃/MoSe₂ nanocomposite

MoO₃/MoSe₂ was prepared by a two-step hydrothermal method. During the synthesis of MoSe₂, before the mixture was transferred to autoclave, a quantitative MoO₃ suspension synthesized by a hydrothermal method was added. The above mixed solution was sonicated for 2 h, then transferred to a 100 mL autoclave. MoO₃/MoSe₂ composite material was finally obtained. The synthesis process is shown in Fig. 1.

2.3. Characterization and measurement

The MoO₃/MoSe₂ suspension was spin coat on the surface of the interdigitated electrode by a spin coating process, and then the aging treatment was performed on the obtained sensor device at room temperature. For better studying the performance characteristics of thin film devices and analyzing the materials from microscopic perspective, X-ray diffractometer (XRD), scanning electron microscope (SEM), transmission electron microscope (TEM), X-ray photoelectron spectroscope (XPS) and other precision equipment were used to characterize the sensor materials. The sensor performances were studied by exposure to different concentrations of target gases at RT. The sensor resistance will change due to the change of the target gas concentration. The data were recorded by the Agilent data acquisition instrument (Agilent 34970A) and uploaded to PC via the RS-232 bus, which could then be stored,

analyzed and processed. The sensor performance is represented by the response calculated by $S = 100\% \times (R_a - R_g) / R_a$. Here, R_a and R_g represent sensor resistance values in air and target gas, respectively.

3. Results And Discussion

3.1 Materials characterization

XRD characterization diagrams of MoSe_2 , MoO_3 and $\text{MoO}_3/\text{MoSe}_2$ heterostructure are shown in Fig. 2, with a test angle range from 10° to 60° . From the XRD pattern of MoO_3 , three high-intensity diffraction peaks can be observed, which indicates that MoO_3 is a highly ordered orthorhombic crystal [23]. The angles of all diffraction peaks of MoO_3 are 13.2° , 23.8° , 26.1° , 27.4° , 38.6° , 42.3° , 46.6° and 53.3° , respectively, which correspond to the (020), (110), (040), (021), (060), (141), (200) and (211) crystal planes of MoO_3 [24]. The XRD confirms that the synthesized MoO_3 contains no other impurities. In the XRD pattern of MoSe_2 , the peaks at 14.1° , 33.2° , 37.1° and 55.9° correspond to the (002), (100), (103) and (110) crystal planes of MoSe_2 [25]. The black line in the figure contains the characteristic diffraction peaks of MoSe_2 and MoO_3 , which shows that the $\text{MoO}_3/\text{MoSe}_2$ heterostructure has been successfully synthesized.

SEM characterization was performed to further verify the successful preparation and visually observe the morphology of the prepared materials. Figure 3 shows the SEM characterization results of MoSe_2 , MoO_3 and $\text{MoO}_3/\text{MoSe}_2$ heterostructure. It can be found from Fig. 3 (a) that MoSe_2 is flower-shaped structure as a whole, and it has a porous structure. The surface of MoO_3 in Fig. 3 (b) has a high degree of crystallinity, and its overall shape is a long rod. Figures 3 (c-d) are SEM characterizations of the $\text{MoO}_3/\text{MoSe}_2$ heterostructure. We can clearly observe the tightly coupled morphology of the two, indicating the successful synthesis of the two materials.

TEM characterization of the prepared materials is shown in Fig. 4. Figure 4 (a) is the micro-morphology of the $\text{MoO}_3/\text{MoSe}_2$ heterostructure. It can be observed that the aggregated flower-like shaded part is MoSe_2 , and the rod-shaped object on the upper right is MoO_3 , which shows that the two substances have been combined together closely. Figure 4 (b) is the TEM characterization diagram of MoO_3 . The rod-shaped MoO_3 morphology can be clearly seen, and its width is about 400 nm. The inset is the electron diffraction pattern (SAED) of partial region of single MoO_3 . Figure 4 (c) is TEM characterization diagram of MoSe_2 . It can be found that MoSe_2 is flower-like shape composed of thin layers. The inset is the SAED of partial area of single MoSe_2 . Figures 4 (d-e) are HRTEM characterization diagrams of MoO_3 and MoSe_2 , respectively. The lattice fringe spacings of 0.33 and 0.41 nm correspond to the (021) and (200) crystal planes of MoO_3 , respectively. The spacings of 0.28 and 0.67 nm correspond to the (100) and (002) crystal planes of MoSe_2 , respectively [26 – 27]. In order to clearly observe the atomic distribution on the surface of MoSe_2 , some designated areas in Fig. 4 (e) are enlarged, as shown in Fig. 4 (f). The MoSe_2

surface exhibits periodic honeycomb structure, which shows that the prepared MoSe₂ has a graphene-like planar structure [25].

Figure 5 is XPS characterization result of MoO₃/MoSe₂ heterostructure. The XPS full spectrum in Fig. 5 (a) indicates that the sample contains elements of Mo, Se, O, and a small amount of C. The source of C may be some organic contaminants remaining on the surface of the sample. Figure 5 (b) shows the spectrum of Mo element. The characteristic peaks appearing at 232.17 and 229.02 eV correspond to the Mo 3d_{3/2} and Mo 3d_{5/2} orbitals of molybdenum tetravalent, respectively, and it is because that MoSe₂ contains Mo-Se bonds [28]. While in MoO₃, the characteristic peaks at 236.18 and 233.05 eV correspond to Mo 3d_{3/2} and Mo 3d_{5/2} orbitals of hexavalent molybdenum, respectively [29]. The characteristic peaks at 55.35 and 54.45 eV in Fig. 5 (c) respectively correspond to the Se 3d_{3/2} and Se 3p_{5/2} orbits of Se²⁻ [28]. Figure 5 (d) is the spectrum of O element, in which the low binding energy of 530.75 eV is derived from the Mo-O bond in MoO₃, and the high binding energy of 531.25 eV corresponds to the oxygen adsorbed on the sample surface [29]. The XPS characterization results also prove the successful synthesis of the composite materials.

3.2 Sensing performance

The experiment results of the sensors on exposure to different concentrations of trimethylamine at RT are shown in Fig. 6. Figure 6 (a) is the dynamic response diagram of MoSe₂ sensor and MoO₃/MoSe₂ heterostructure sensor switching back and forth in air and TMA from 20 to 1000 ppb. Both sensors have good response and recovery characteristics, but MoO₃/MoSe₂ nanocomposite sensor shows higher response values at the same concentration of TMA gas. Moreover, MoO₃/MoSe₂ sensor can detect TMA as low as 20 ppb with high sensitivity, whose response is as high as 19%. Figure 6 (b) shows the fitting curves of the response values and gas concentrations of the two. Among them, the fitting curve of MoO₃/MoSe₂ heterostructure sensor is $Y = 6.1861X^{0.3544}$, and the regression coefficient R^2 is 0.9912. The response fitting curve of MoSe₂ sensor is $Y = 1.6909X^{0.4396}$, and R^2 is 0.9856. Figure 6 (c) is the dynamic resistance change of MoO₃/MoSe₂ nanocomposite sensor. When the sensor is switched from air to trimethylamine environment, its resistance values emerge a downward trend, which shows that the sensor as a whole is n-type. Figure 6 (d) shows the response/recovery characteristics of two sensors to 1000 ppb TMA. It is not difficult to find that MoO₃/MoSe₂ nanocomposite sensor not only has a higher response value, but also has a faster response speed, which further illustrates that the MoO₃/MoSe₂ heterostructure helps to improve the gas sensing performance.

Figure 7 (a) shows the long-term stability of MoO₃/MoSe₂ nanocomposite sensor. Every two days, the sensor was tested on exposure to different concentrations (50, 250 and 500 ppb) of TMA, and the results show that the sensor is stable enough. When studying sensor performances, it is necessary to explore the effect of humidity on sensor response. Figure 7 (b) is the fitting curve of the response of MoO₃/MoSe₂ heterostructure sensor to 250 ppb TMA under different humidity conditions. The fitting equation is $Y =$

55.672 - 0.215X, where the horizontal axis X is relative humidity, vertical axis Y is the response value of the sensor, and the regression coefficient R^2 is 0.939, which shows that the influence of humidity on the sensor is regular. The repeatability test was also performed on the sensor, as shown in Fig. 7 (c). $\text{MoO}_3/\text{MoSe}_2$ sensor was tested in air and fixed concentration of TMA gas for five cycles, respectively. The experimental results show that the sensor has good recoverability. The selectivity of the sensor to target gas is very important. As shown in Fig. 7 (d), compared with other interfering gases, $\text{MoO}_3/\text{MoSe}_2$ nanocomposite sensor and MoSe_2 sensor have higher response values to TMA, indicating that test sensors have good selectivity to TMA.

Table 1 lists the comparison of TMA response characteristics among $\text{MoO}_3/\text{MoSe}_2$ based sensor in this work and previously reported sensors. It can be found that compared with the previous reported TMA sensors, the $\text{MoO}_3/\text{MoSe}_2$ sensor not only has a very low detection limit and higher response, but also has a lower working temperature, which can be used in room temperature. Therefore, the sensor proposed in this paper can be an excellent candidate for TMA detection.

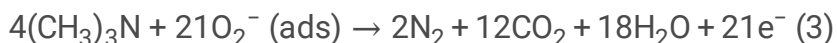
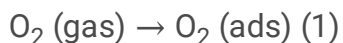
Table 1
Comparison of TMA sensing performance of as-fabricated $\text{MoO}_3/\text{MoSe}_2$ based sensor against previous reported results.

Materials	Working Temp.	Response	LOD	Ref.
Pd-ZnO	300°C	2.9 (1 ppm)	1 ppm	[1]
$\alpha\text{-MoO}_3$	133°C	1.25 (20 ppb)	20 ppb	[12]
V_2O_5	240°C	2.8 (100 ppm)	10 ppm	[30]
$\text{MoO}_3/\text{Bi}_2\text{Mo}_3\text{O}_{12}$	170°C	7.2 (10 ppm)	100 ppb	[32]
$\text{V}_2\text{O}_3\text{-Cu}_2\text{O}$	RT	1.08 (3 ppm)	3 ppm	[33]
$\text{Co}_3\text{O}_4/\text{SnO}_2$	175°C	9.3 (5 ppm)	1 ppm	[34]
3D rGO/ In_2O_3	RT	9.3% (100 ppm)	100 ppm	[35]
CdO:Al	RT	32.12% (300 ppm)	50 ppm	[36]
$\text{MoO}_3/\text{MoSe}_2$	RT	19% (20 ppb)	20 ppb	This work

3.3 Gas sensing mechanism

The schematic diagram of the TMA sensing mechanism of $\text{MoO}_3/\text{MoSe}_2$ sensor is shown in Fig. 8. As a typical n-type semiconductor, the carriers of MoO_3 are electrons. It is known from the above gas-sensitivity test results that the MoSe_2 based sensor also exhibits n-type semiconductor characteristics to TMA. In gas sensing process, the $\text{MoO}_3/\text{MoSe}_2$ heterostructure does not participate in the reaction, it is the oxygen ions adsorbed on the surface that do. In other words, the gas sensing mechanism benefits

from the adsorption and desorption of oxygen on the sensor surface. Possible reactions are as follows [31, 36]:



It can be seen that when the sensor device is transferred from air to TMA environment, a large amount of electrons will be released, so the sensor exhibits lower resistance value. There may be two reasons for the enhanced gas sensing performance of MoO₃/MoSe₂ heterostructure sensor. Firstly, MoO₃/MoSe₂ composite structure has a large specific surface area [37 – 38], which is conducive to the diffusion of TMA molecules and makes TMA react with adsorbed oxygen thoroughly, thereby enhancing the gas sensing response. Secondly, the heterostructure formed between MoO₃ and MoSe₂ has synergistic effect. The formation of the heterostructure has an effect on the conductivity of the sensor. After MoO₃ is modified with MoSe₂ to form the heterostructure, the resistance value of the sensor in air decreases, meaning that the conductivity of the device is improved, which is conducive to the rapid conduction of carriers. The energy band diagram at the interface between MoO₃ and MoSe₂ and the formation process of the heterostructure are studied, as shown in Fig. 9. Figure 9 (a) is the energy band diagram before the two substances are combined, in which the band gap of MoO₃ and MoSe₂ are 3.2 and 1.3 eV, the work function is 6.9 and 4.6 eV, and the electron affinity is 6.7 and 3.9 eV, respectively [39 – 40]. Figure 9 (b) shows the formation process of the n-n heterostructure in air. At this time, the electron transfer between the two causes the energy band to bend. The change process of the heterostructure in TMA is shown in Fig. 9 (c). The width of the depletion layer is narrowed due to the reaction between TMA and the adsorbed oxygen, so that the sensor shows higher response value and faster response speed.

4. Conclusions

In summary, TMA sensor based on MoO₃/MoSe₂ n-n heterostructure was proposed in this paper. The microstructures of MoO₃/MoSe₂ nanocomposite were characterized by various characterization methods, and the gas sensing properties of MoSe₂ and MoO₃/MoSe₂ nanocomposite sensors were also tested. The MoO₃/MoSe₂ nanocomposite was composed of MoSe₂ and MoO₃, in which MoSe₂ possessed a porous flower-shaped structure, and MoO₃ had a long rod structure. The experimental results showed that compared with the single sensing material, the MoO₃/MoSe₂ sensor had more excellent sensing performance, which could detect low concentration of TMA gas at RT. The enhanced sensing performance was mainly due to the unique morphology and heterostructure of MoO₃/MoSe₂. This work confirmed that the MoO₃/MoSe₂ composite sensor was a good choice for TMA detection.

Declarations

Acknowledgements

This work was supported by the Independent Innovation Scientific Research Project of China University of Petroleum (East China) (20CX06065A) and China Postdoctoral Science Foundation (2020M682263).

Notes

The authors declare no competing financial interest.

References

1. D. Meng, D. Liu, S. Wang, Y. Shen, X. San, J. Si, F. Meng, In-situ growth of ordered Pd-doped ZnO nanorod arrays on ceramic tube with enhanced trimethylamine sensing performance. *Appl. Surf. Sci.* **463**, 348–356 (2019)
2. S. Park, B. Kim, Y. Jo, Z. Dai, J. Lee, Chemiresistive trimethylamine sensor using monolayer SnO₂ inverse opals decorated with Cr₂O₃ nanoclusters. *Sens. Actuators, B* **309**, 127805 (2020)
3. Y. Cho, X. Liang, Y. Kang, J. Lee, Ultrasensitive detection of trimethylamine using Rh-doped SnO₂ hollow spheres prepared by ultrasonic spray pyrolysis. *Sens. Actuators, B* **207**, 330–337 (2015)
4. L. Balino-Zuazo, A. Barranco, A novel liquid chromatography-mass spectrometric method for the simultaneous determination of trimethylamine, dimethylamine and methylamine in fishery products. *Food Chem.* **196**, 1207–1214 (2016)
5. X. Chu, J. Wang, Q. Gao, Y. Wang, S. Liang, L. Bai, Y. Dong, M. Epifani, High selectivity trimethylamine sensors based on graphene-NiGa₂O₄ nanocomposites prepared by hydrothermal method. *Physica E* **118**, 113788 (2020)
6. S. Shen, X. Zhang, X. Cheng, Y. Xu, S. Gao, H. Zhao, X. Zhou, L. Huo, Oxygen-vacancy-enriched porous α-MoO₃ nanosheets for trimethylamine sensing. *ACS Appl. Nano Mater.* **2**, 8016–8026 (2019)
7. F. Ji, X. Ren, X. Zheng, Y. Liu, L. Pang, J. Jiang, S. Liu, 2D-MoO₃ nanosheets for superior gas sensors. *NANOSCALE* **8**, 8696 (2016)
8. L. Zhang, Z. Liu, L. Jin, B. Zhang, H. Zhang, M. Zhu, W. Yang, Self-assembly gridding-MoO₃ nanobelts for highly toxic H₂S gas sensors. *Sens. Actuators, B* **237**, 350–357 (2016)
9. J. Shen, S. Guo, C. Chen, L. Sun, S. Wen, Y. Chen, S. Ruan, Synthesis of Ni-doped-MoO₃ nanolamella and their improved gas sensing properties. *Sens. Actuators, B* **252**, 757–763 (2017)
10. S. Wang, J. Xie, J. Hu, H. Qin, Y. Cao, Fe-doped α-MoO₃ nanoarrays: Facile solid-state synthesis and excellent xylene-sensing performance. *Appl. Surf. Sci.* **512**, 145722 (2020)
11. H. Li, L. Huang, X. Wang, C. Lee, J. Yoon, J. Zhou, X. Guo, J. Lee, Molybdenum trioxide nanopaper as a dual gas sensor for detecting trimethylamine and hydrogen sulfide. *RSC Adv.* **7**, 3680–3685 (2017)
12. S. Yang, Y. Liu, W. Chen, W. Jin, J. Zhou, H. Zhang, G. Zakharova, High sensitivity and good selectivity of ultralong MoO₃ nanobelts for trimethylamine gas. *Sens. Actuators, B* **226**, 478–485 (2016)

13. S. Mao, Z. Wen, S. Ci, X. Guo, K. Ostrikov, J. Chen, Perpendicularly oriented MoSe₂/graphene nanosheets as advanced electrocatalysts for hydrogen evolution. *SMALL* **11**, 414–419 (2015)
14. S. Deng, Y. Zhong, Y. Zeng, Y. Wang, Z. Yao, F. Yang, S. Lin, X. Wang, X. Lu, X. Xia, J. Tu, Directional construction of vertical nitrogen-doped 1T-2H MoSe₂/graphene shell/core nanoflake arrays for efficient hydrogen evolution reaction. *Adv. Mater.* **29**, 1700748 (2017)
15. S. Deng, F. Yang, Q. Zhang, Y. Zhong, Y. Zeng, S. Lin, X. Wang, X. Lu, C. Wang, L. Gu, X. Xia, J. Tu, Phase modulation of (1T-2H)-MoSe₂/TiC-C shell/core arrays via nitrogen doping for highly efficient hydrogen evolution reaction. *Adv. Mater.* **30**, 1802223 (2018)
16. Y. Wu, M. Xu, X. Chen, S. Yang, H. Wu, J. Pan, X. Xiong, CTAB-assisted synthesis of novel ultrathin MoSe₂ nanosheets perpendicular to graphene for the adsorption and photodegradation of organic dyes under visible light. *NANOSCALE* **8**, 440–450 (2016)
17. X. Yang, Z. Zhang, Y. Fu, Q. Li, Porous hollow carbon spheres decorated with molybdenum diselenide nanosheets as anodes for highly reversible lithium and sodium storage. *NANOSCALE* **7**, 10198–10203 (2015)
18. J. Ge, L. Fan, J. Wang, Q. Zhang, Z. Liu, E. Zhang, Q. Liu, X. Yu, B. Lu, MoSe₂/N-doped carbon as anodes for potassium-ion batteries. *Adv. Energy Mater.* **8**, 1801477 (2018)
19. B. Kirubasankar, S. Vijayan, S. Angaiah, Sonochemical synthesis of a 2D-2D MoSe₂/graphene nanohybrid electrode material for asymmetric supercapacitors. *Sustainable energy fuels* **3**, 467–477 (2019)
20. S. Zhang, T. Nguyen, W. Zhang, Y. Park, W. Yang, Correlation between lateral size and gas sensing performance of MoSe₂ nanosheets. *Appl. Phys. Lett.* **111**, 161603 (2017)
21. X. Chen, X. Chen, Y. Han, C. Su, M. Zeng, N. Hu, Y. Su, Z. Zhou, H. Wei, Z. Yang, Two-dimensional MoSe₂ nanosheets via liquid-phase exfoliation for high-performance room temperature NO₂ gas sensors. *Nanotechnology* **30**, 445503 (2019)
22. D. Zhang, Q. Li, P. Li, M. Pang, Y. Luo, Fabrication of Pd-decorated MoSe₂ nanoflowers and density functional theory simulation toward ammonia sensing. *IEEE Electron Device Lett.* **40**, 616–619 (2019)
23. B. Yao, L. Huang, J. Zhang, X. Gao, J. Wu, Y. Cheng, X. Xiao, B. Wang, Y. Li, J. Zhou, Flexible transparent molybdenum trioxide nanopaper for energy storage. *Adv. Mater.* **28**, 6353–6358 (2016)
24. Z. Li, W. Wang, Z. Zhao, X. Liu, P. Song, One-step hydrothermal preparation of Ce-doped MoO₃ nanobelts with enhanced gas sensing properties. *RSC Adv.* **7**, 28366 (2017)
25. J. Huang, B. Jin, H. Liu, X. Li, Q. Zhang, S. Chu, R. Peng, S. Chu, Controllable synthesis of flower-like MoSe₂ microspheres for highly efficient visible-light photocatalytic degradation of nitro-aromatic explosives. *J. Mater. Chem. A* **6**, 11424 (2018)
26. H. Li, L. Huang, X. Wang, C. Lee, J. Yoon, J. Zhou, X. Guo, J. Lee, Molybdenum trioxide nanopaper as a dual gas sensor for detecting trimethylamine and hydrogen sulfide. *RSC Adv.* **7**, 3680 (2017)

27. D. Zeng, P. Wu, W. Ong, B. Tang, M. Wu, H. Zheng, Y. Chen, D. Peng, Construction of network-like and flower-like 2H-MoSe₂ nanostructures coupled with porous g-C₃N₄ for noble-metal-free photocatalytic H₂ evolution under visible light. *Appl. Catal. B* **233**, 26–34 (2018)
28. J. Zhang, W. Kang, M. Jiang, Y. You, Y. Cao, T. Ng, D. Yu, C. Lee, J. Xu, Conversion of 1T-MoSe₂ to 2H-MoS₂xSe_{2-2x} mesoporous nanospheres for superior sodium storage performance. *Nanoscale* **9**, 1484–1490 (2017)
29. X. Wang, Y. Zhang, Z. Chen, Effect of MoO₃ constituents on the growth of MoS₂ nanosheets by chemical vapor deposition. *Mater. Res. Express* **3**, 065014 (2016)
30. D. Wang, K. Gu, Q. Zhao, C. Zhai, T. Yang, Q. Lu, J. Zhang, M. Zhang, Synthesis and trimethylamine sensing properties of spherical V₂O₅ hierarchical structures. *New J. Chem* **42**, 14188 (2018)
31. F. Zhang, X. Dong, X. Cheng, Y. Xu, X. Zhang, L. Huo, Enhanced gas-sensing properties for trimethylamine at low temperature based on MoO₃/Bi₂Mo₃O₁₂ hollow microspheres. *ACS Appl. Mater. Interfaces* **11**, 11755–11762 (2019)
32. V. Mounasamy, G. Mani, D. Ponnusamy, K. Tsuchiya, A. Prasad, S. Madanagurusamy, Sub-ppm level detection of trimethylamine using V₂O₃-Cu₂O mixed oxide thin films. *Ceram. Int.* **45**, 19528–19533 (2019)
33. D. Meng, J. Si, M. Wang, G. Wang, Y. Shen, X. San, F. Meng, One-step synthesis and the enhanced trimethylamine sensing properties of Co₃O₄/SnO₂ flower-like structures. *Vacuum* **171**, 108994 (2020)
34. Z. Ma, P. Song, Z. Yang, Q. Wang, Trimethylamine detection of 3D rGO/mesoporous In₂O₃ nanocomposites at room temperature. *Appl. Surf. Sci.* **465**, 625–634 (2019)
35. B. Balachandar, T. Logu, R. Ramprasath, K. Sankarasubramanian, P. Soundarrajan, M. Sridharan, K. Ramamurthi, K. Sethuraman, Spray pyrolysis deposited CdO: Al films for trimethylamine sensing application. *Mater. Sci. Semicond. Process.* **105**, 104753 (2020)
36. Q. Qi, Y. Zou, M. Fan, Y. Liu, S. Gao, P. Wang, Y. He, D. Wang, G. Li, Trimethylamine sensors with enhanced anti-humidity ability fabricated from La_{0.7}Sr_{0.3}FeO₃ coated In₂O₃-SnO₂ composite nanofibers. *Sens. Actuators, B* **203**, 111–117 (2014)
37. Y. Luo, S. Hu, H. Wang, Y. Chen, J. Dong, Z. Jiang, X. Xiong, W. Zhu, W. Qiu, H. Lu, H. Guan, Y. Zhong, J. Yu, J. Zhang, Z. Chen, Sensitivity-enhanced surface plasmon sensor modified with MoSe₂ overlayer. *Opt. Express* **26**, 34250–34258 (2016)
38. N. Vishnu, S. Badhulika, Single step synthesis of MoSe₂-MoO₃ heterostructure for highly sensitive amperometric detection of nitrite in water samples of industrial areas. *Electroanalysis* **31**, 2410–2416 (2019)
39. Z. Yang, D. Zhang, D. Wang, Carbon monoxide gas sensing properties of metal-organic frameworks-derived tin dioxide nanoparticles/molybdenum diselenide nanoflowers. *Sens. Actuators, B* **304**, 127369 (2020)
40. Z. Li, P. Song, Z. Yang, Q. Wang, In situ formation of one-dimensional CoMoO₄/MoO₃ heterojunction as an effective trimethylamine gas sensor. *Ceram. Int.* **44**, 3364–3370 (2018)

Figures

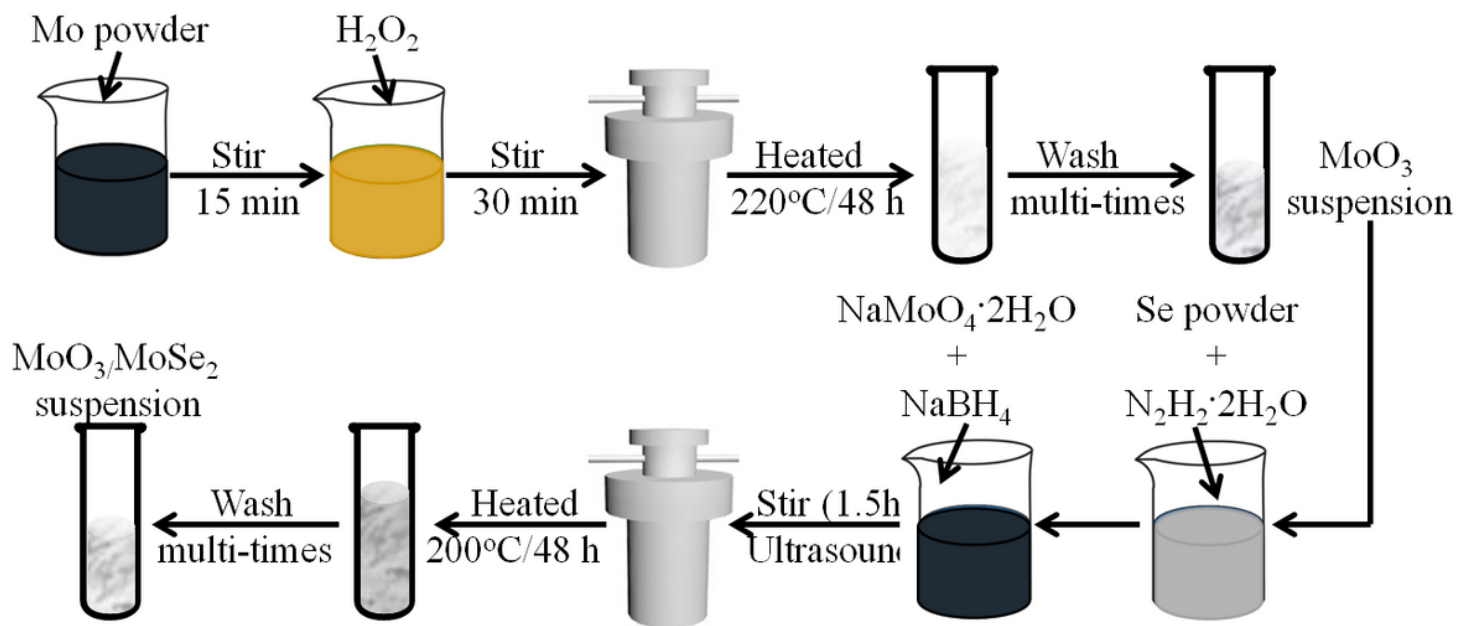


Figure 1

Manufacturing process of $\text{MoO}_3/\text{MoSe}_2$ nanocomposite.

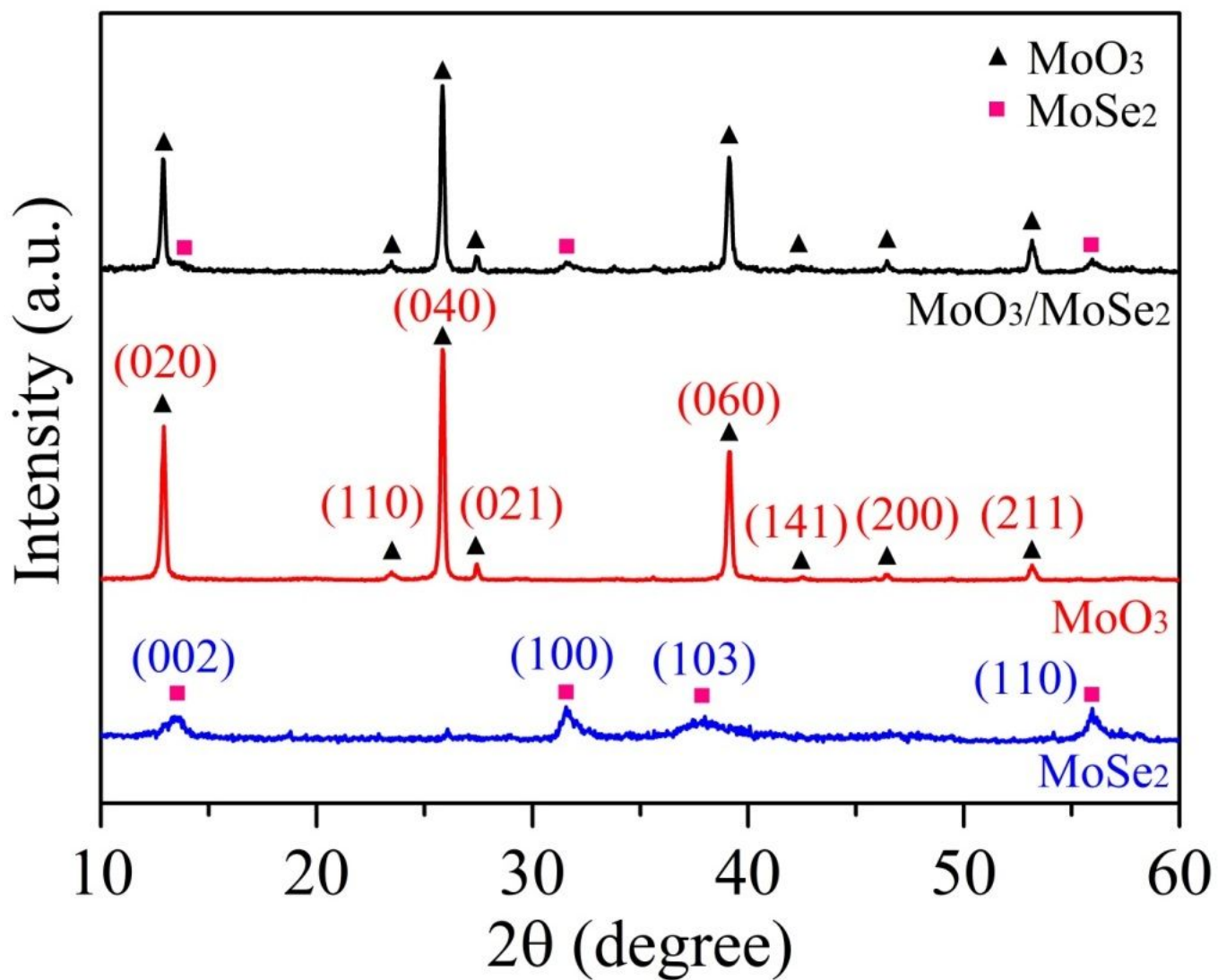


Figure 2

XRD patterns of MoSe₂, MoO₃ and MoO₃/MoSe₂ nanocomposite.

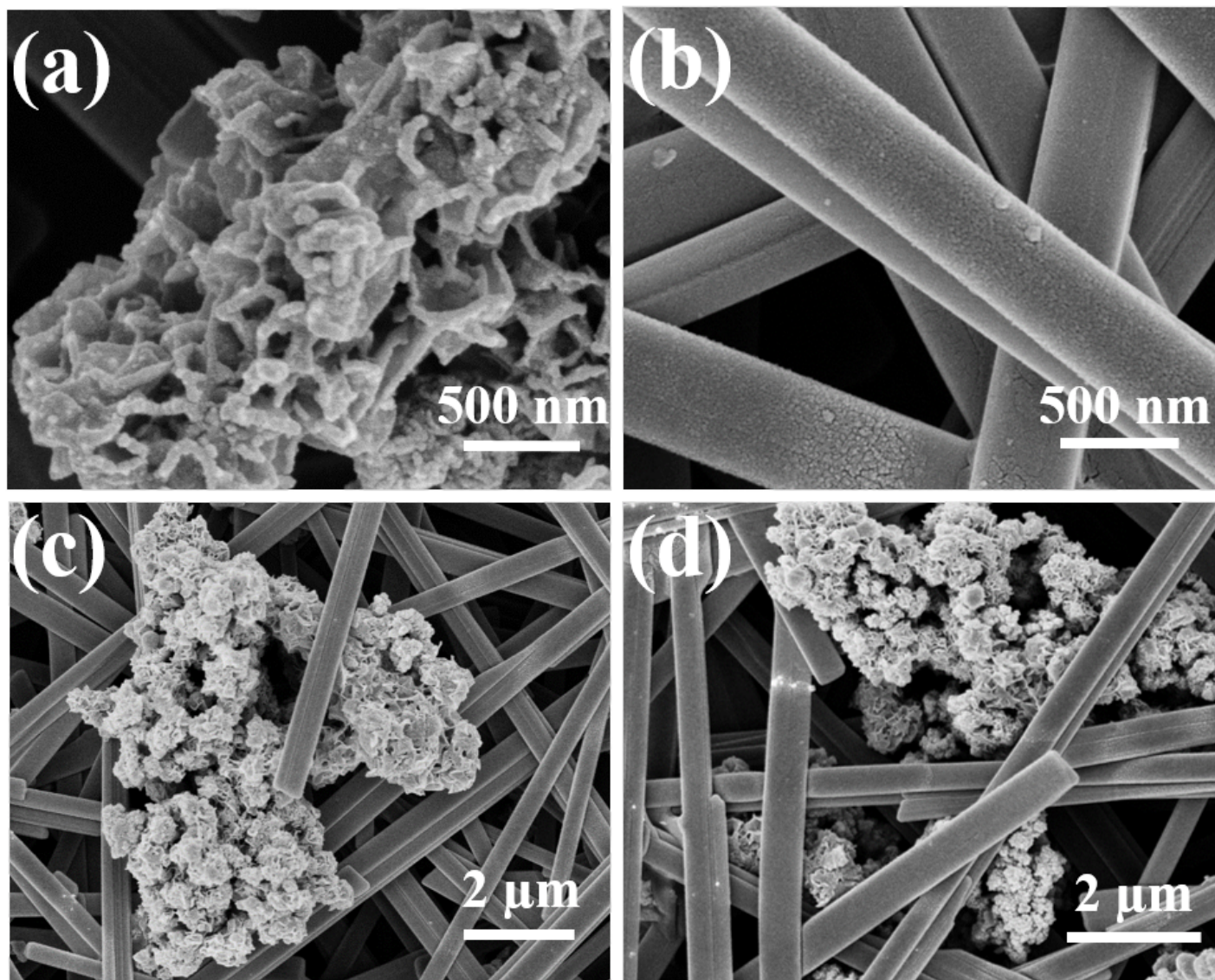


Figure 3

SEM characterization: (a) MoSe₂, (b) MoO₃, and (c-d) MoO₃/MoSe₂ nanocomposite.

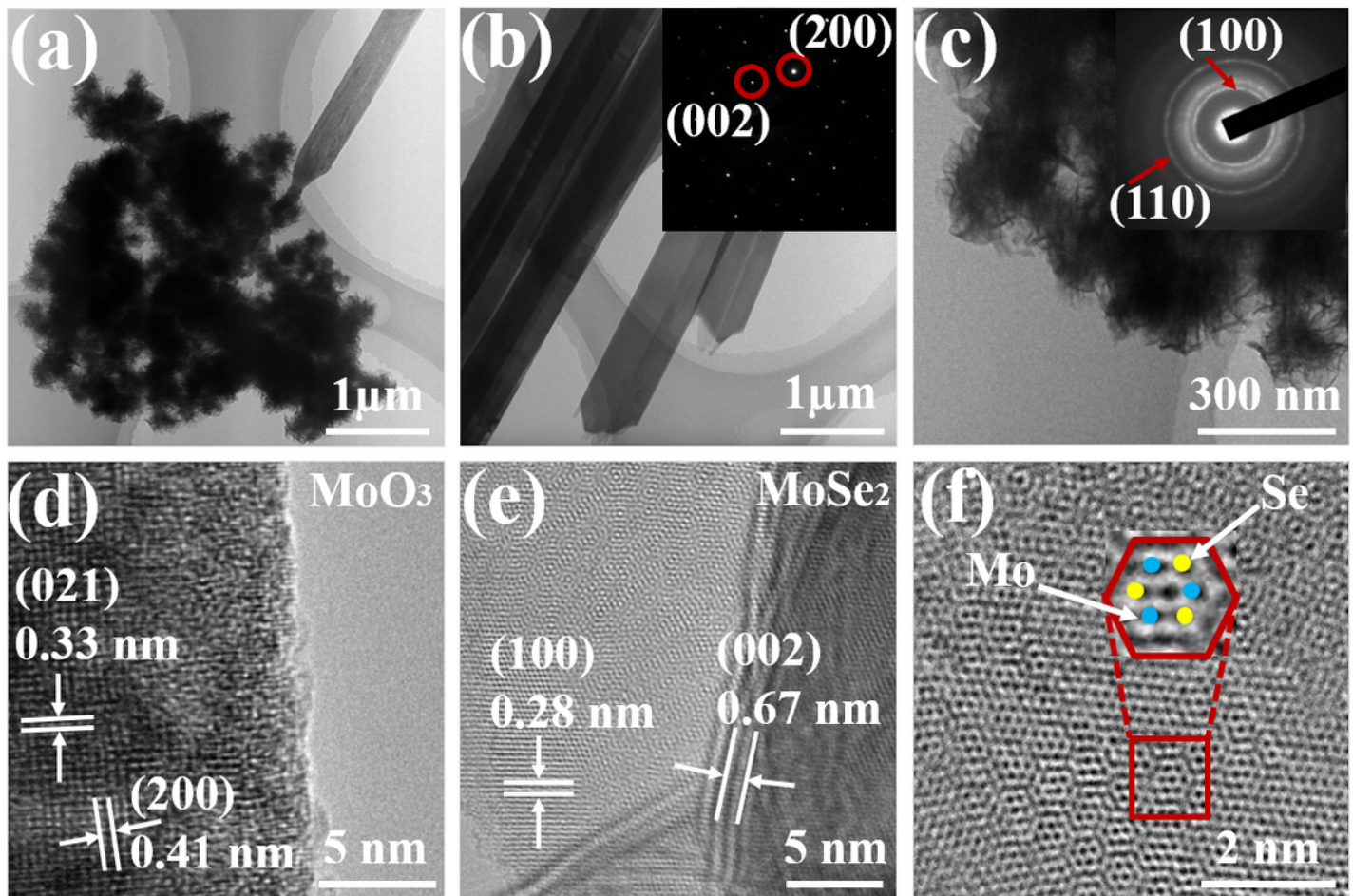


Figure 4

TEM characterization: (a) MoO₃/MoSe₂, (b-c) MoO₃ and MoSe₂. The inset is the electron diffraction pattern (SAED). (d-e) High-resolution TEM images of MoO₃/MoSe₂ nanocomposite. (f) Schematic diagram of the surface atomic distribution of MoSe₂.

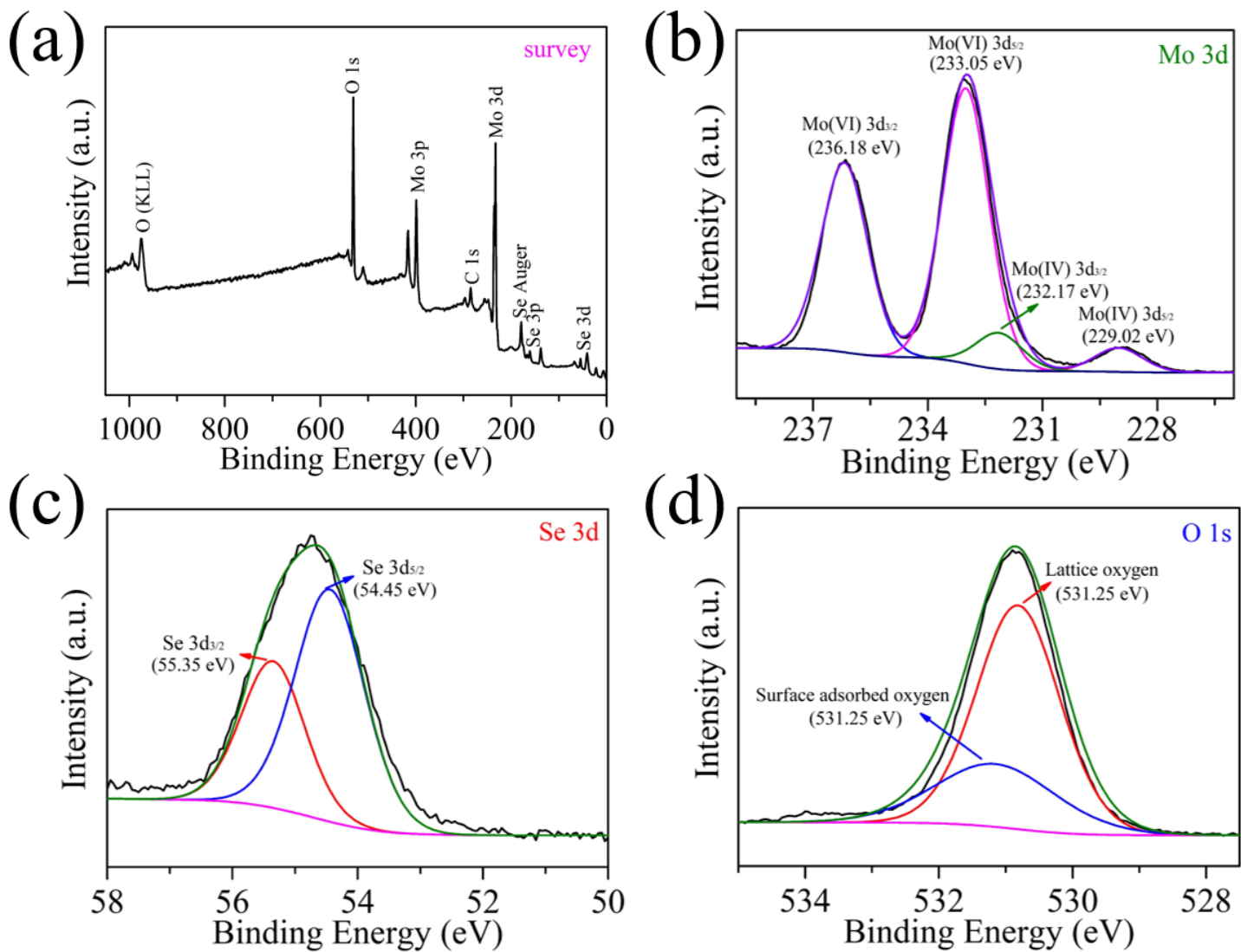


Figure 5

XPS spectra of MoO₃/MoSe₂ nanocomposite: (a) survey, (b) Mo 3d, (c) Se 3d, and (d) O 1s.

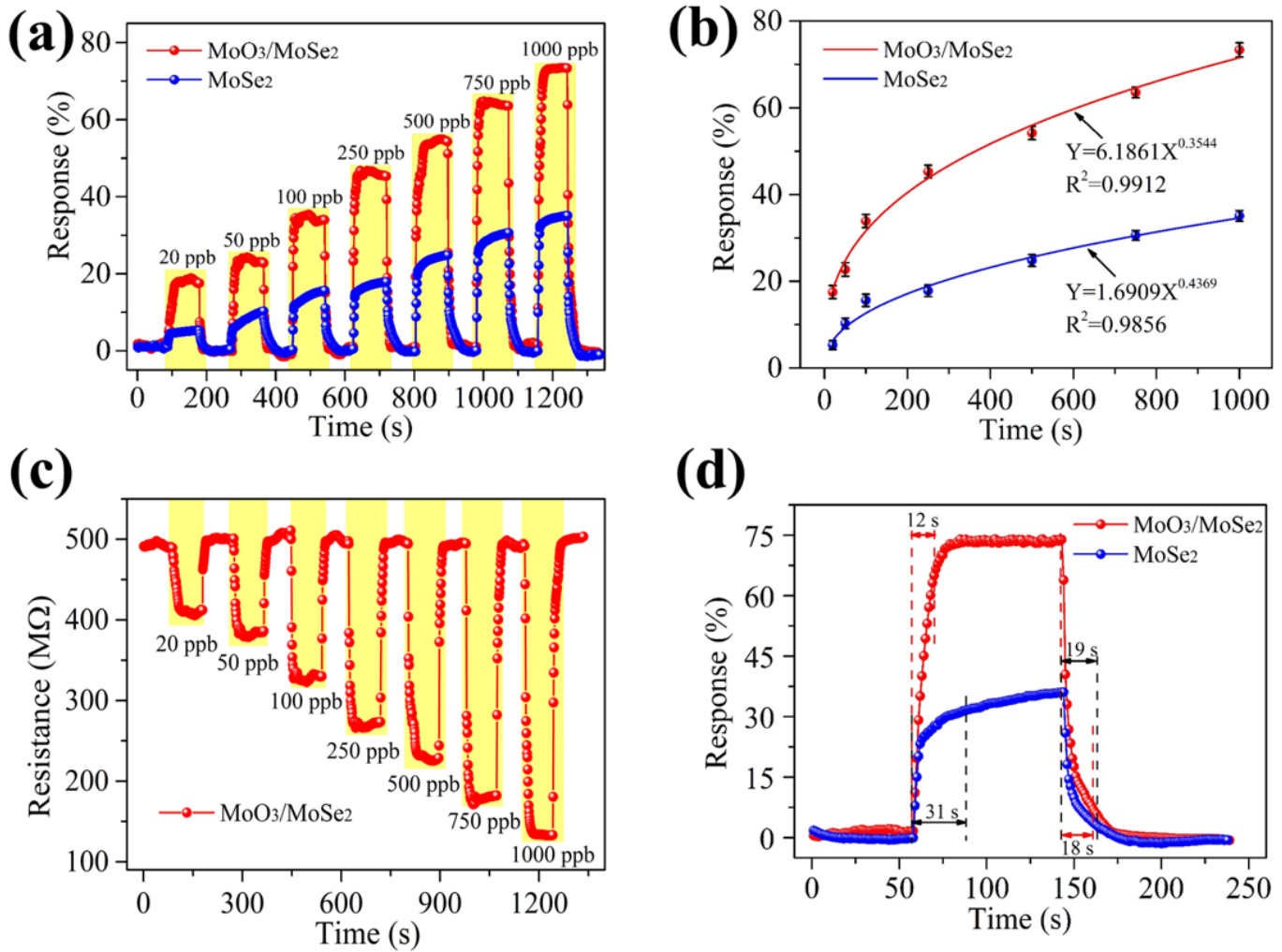


Figure 6

MoSe₂ and MoO₃/MoSe₂ nanocomposite sensors at room temperature. (a) Plot of sensor response as a function of time. (b) Plot of sensor response as a function of gas concentration. (c) Dynamic resistance change of MoO₃/MoSe₂ nanocomposite sensor. (d) Response/recovery characteristics of the two sensors to 1000 ppb TMA.

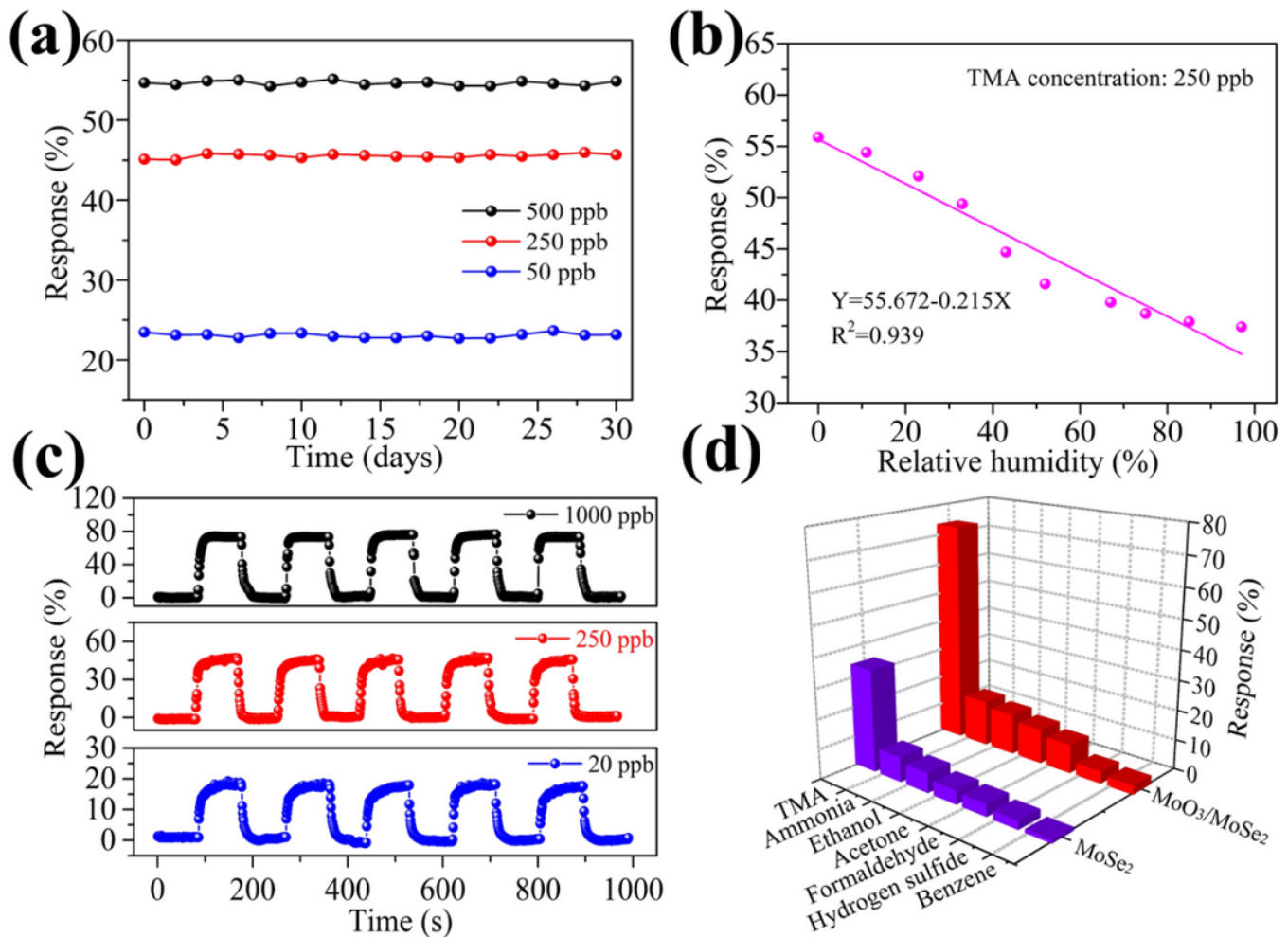


Figure 7

MoSe₂ and MoO₃/MoSe₂ sensors at room temperature. (a) Long-term stability test of MoO₃/MoSe₂ sensor. (b) Fit curve of relative humidity and MoO₃/MoSe₂ sensor response in 250 ppb TMA. (c) Repeatability test results of MoO₃/MoSe₂ sensor. (d) Selectivity test results of MoSe₂ sensor and MoO₃/MoSe₂ nanocomposite sensor in 1000 ppb concentration of different detected gases.

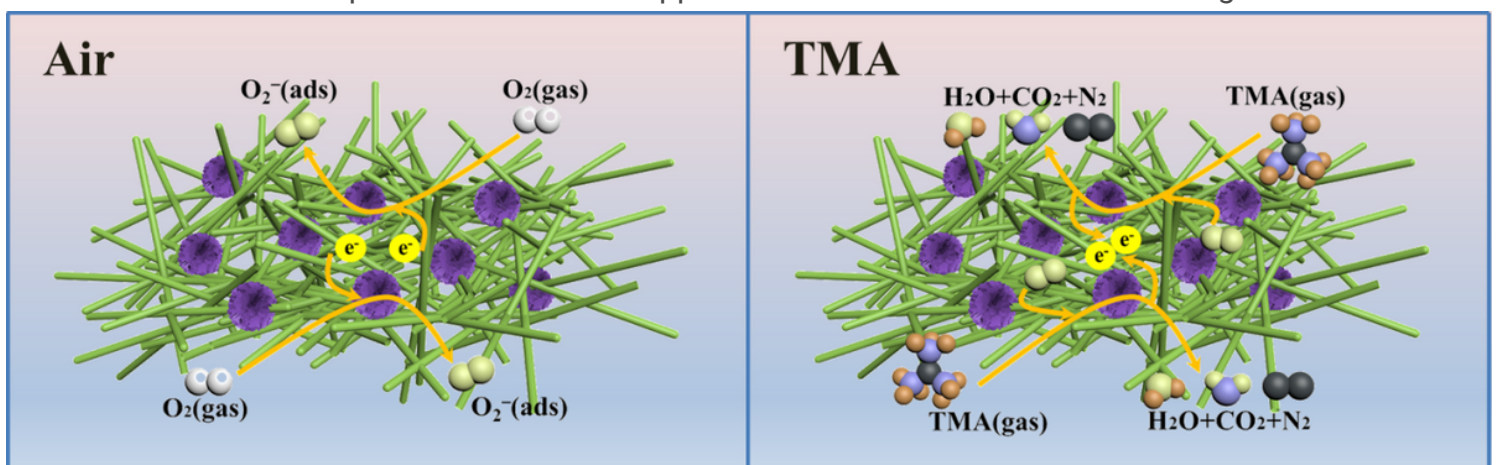


Figure 8

Schematic diagram of TMA sensing mechanism of MoO₃/MoSe₂ sensor.

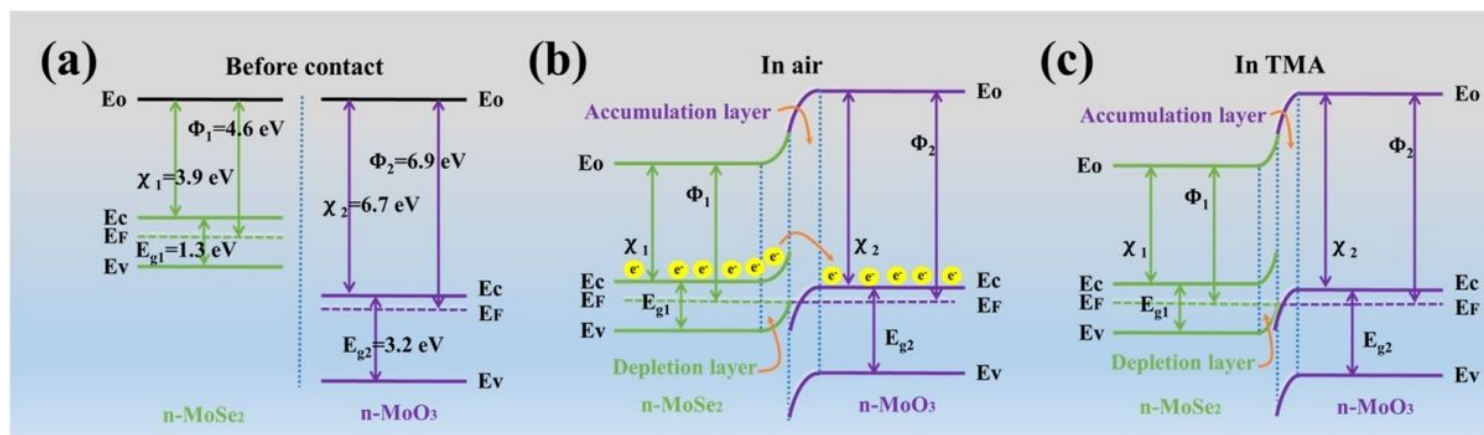


Figure 9

Energy band diagrams of MoO₃/MoSe₂ nanocomposite: (a) before contact, (b) in air, and (c) TMA.